SANDIA REPORT
SAND2003-8732
Unlimited Release
Printed December 2003

First Principles Determination of Dislocation Properties

J. C. Hamilton

Prepared by
Sandia National Laboratories
Albuquerque, New Mexico 87185 and Livermore, California 94550

Sandia is a multiprogram laboratory operated by Sandia Corporation,
a Lockheed Martin Company, for the United States Department of Energy's
National Nuclear Security Administration under Contract DE-AC04-94AL85000.

Sandia National Laboratories

Issued by Sandia National Laboratories, operated for the United States Department of Energy by Sandia Corporation.

Available to DOE and DOE contractors from
U.S. Department of Energy
Office of Scientific and Technical Information
P.O. Box 62
Oak Ridge, TN 37831

Telephone: (865)576-8401
Facsimile: (865)576-5728
E-Mail: reports@adonis.osti.gov
Online ordering: http://www.doe.gov/bridge

Available to the public from
U.S. Department of Commerce
National Technical Information Service
5285 Port Royal Rd
Springfield, VA 22161

Telephone: (800)553-6847
Facsimile: (703)605-6900
E-Mail: orders@ntis.fedworld.gov
Online order: http://www.ntis.gov/help/ordermethods.asp?loc=7-4-0#online

SAND2003-8732
Unlimited Release
Printed December 2003

First Principles Determination of Dislocation Properties

John C. Hamilton
Materials Physics- Department

Sandia National Laboratories
P. O. Box 969
Livermore, CA 94551-0969

ABSTRACT

This report details the work accomplished on first principles determination of dislocation properties. It contains an introduction and three chapters detailing three major accomplishments. First, we have used first principle calculations to determine the shear strength of an aluminum twin boundary. We find it to be remarkably small (~17 mJ/m^2). This unexpected result is explained and will likely pertain for many other grain boundaries. Second, we have proven that the conventional explanation for finite grain boundary facets is wrong for a particular aluminum grain boundary. Instead of finite facets being stabilized by grain boundary stress, we find them to originate from kinetic effects. Finally we report on a new application of the Frenkel-Kontorova model to understand reconstructions of (100) type surfaces. In addition to the commonly accepted formation of rectangular dislocation arrays, we find numerous other possible solutions to the model including hexagonal reconstructions and a clock-rotated structure.

This page intentionally left blank

CONTENTS

This page intentionally left blank

INTRODUCTION

Dislocations are one of the most fundamental microstructural aspects of materials science. Dislocations are found in bulk materials, in thin films and at surfaces. Dislocations play a major role in determining mechanical and other properties of materials. Study of dislocations using first principles techniques has been a long-standing challenge because the number of atoms in a unit cell is typically large. In this report we discuss three practical examples of multiscale modeling of dislocations based on first principles calculations. This first chapter provides a brief introduction to the rational and to the subjects to be covered.

In the second chapter, we turn to the study of grain boundary shearing. Grain boundaries are often understood and modeled as an array of dislocations. We introduce the concept of a "generalized gamma surface" which can incorporate such phenomena as grain boundary translation during sliding. The generalized gamma surface allows us to calculate the stress required to shear a grain boundary. It also allows us to calculate the width of certain classes of observed dislocation structures.

In the third chapter, we discuss the equilibrium length of facets at a faceted grain boundary. This topic has a major impact in terms of understanding grain boundary phase transitions. We begin by discussing the strain fields which play a major role in determining facet lengths. Because bond lengths tend to be shorter across a grain boundary, there is a translation vector which produces a dislocation at the junction between two grain boundaries. We incorporate these concepts into a continuum elasticity model. Using first principles we calculate the Burger's vector of the grain boundary junctions and the stress of a grain boundary facet. In contrast to present qualitative theory, we find using quantitative first principles methods that the equilibrium length is infinite. This implies that kinetic arguments are the probable cause of observed finite facets.

In the fourth chapter we turn to the subject of dislocation structure for surfaces and thin films. Here we show that the Frenkel-Kontorova model can predict a wide range of dislocation structures for films with square symmetry. We also predict a novel "clock-rotated" structure as a strain relief alternative to dislocations. This structure is verified using first-principles calculations.

This page intentionally left blank

II. First-Principles Calculations of Grain Boundary

Theoretical Shear Strength Using Transition State Finding to Determine Generalized Gamma Surface Cross Sections

The gamma surface for a simple solid-solid interface was originally defined by Vitek.[1] The gamma surface is the excess energy of the interface as the lattice on one side of the interface is translated relative to the lattice on the other side of the interface. The gamma surface is an important concept in the study of interfaces and grain boundaries in solids. As discussed by Sutton and Balluffi,[2] the gamma surface is useful in understanding both grain boundary sliding and the structure of grain boundary dislocations. For low index shear planes in single crystals, the definition and calculation of a gamma surface is relatively straightforward. Typically the atomic coordinates on one side of the interface are rigidly translated, constrained in the directions parallel to the interface, and then relaxed to an energy minimum in the direction perpendicular to the interface.[3] Here we present an example of grain boundary sliding which involves complex cooperative atomic motions in addition to rigid translation of the atoms on the two sides of the grain boundary. In order to quantify the energy of these complex atomic motions, we propose a new concept, the "generalized gamma surface".

In order to discuss the connection between grain boundary sliding, grain boundary gamma surfaces, and transition state finding techniques, we consider a specific example, the Al $\Sigma 3 (11\bar{2})/[1\bar{1}0]$ tilt boundary. We first review methods used in previous first-principles calculations of shearing of bicrystals[4,5] and single crystals.[6] We next show that the apparently simple definition of a gamma surface needs to be modified for some grain boundaries because complex cooperative motions of atoms at the grain boundary can occur as one lattice is translated relative to the lattice on the other side of the grain boundary. We propose the use of recently developed transition-state-finding techniques as an appropriate way to calculate relevant cross sections of the gamma surface for grain boundaries. Finally we apply a first-principles calculation of this type to calculate the theoretical shear strength of the Al $\Sigma 3 (11\bar{2})$ tilt boundary in a bicrystal.

One way to investigate grain boundary sliding is to subject a bicrystal to a shear stress parallel to the grain boundary as shown in figure 2-1. Previous first-principles calculations of grain boundary sliding have used this approach.[4,5] The theoretical shear strength of a perfect single crystal has also been calculated in a similar manner.[6] In drawing figure 2-1, we have assumed that the shear strength of the grain boundary is less than that of the bulk crystal and that the deformation of the bulk grains is purely elastic.

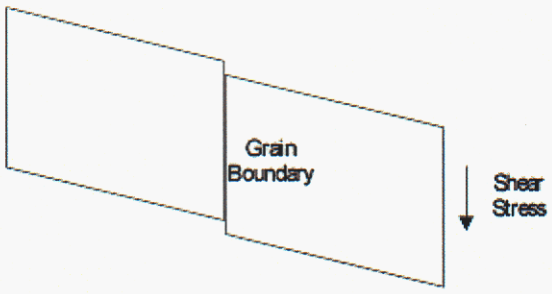

Figure 2-1. Perfect bicrystal subject to a shear stress parallel to the grain boundary. The two bulk grains undergo a shear strain and an offset develops between the two grains. If the shear stress is less that the theoretical shear strength of the grain boundary, the offset between the two grains will be a fraction of the lattice spacing. If the shear stress exceeds the theoretical shear strength of the grain boundary, grain boundary sliding will occur and the offset between the two grains may be many lattice spacings.

This situation has been observed in experiments where the grain boundary shears but the bulk crystal is stable.[7] There are two contributions to the energy of the bicrystal as a function of shear stress. One is the strain energy of the two bulk grains. This energy will scale with the volume of the bicrystal. The other contribution is the energy associated with a displacement between the two grains at the grain boundary, i.e. the gamma surface energy. This energy will scale with the area of the grain boundary. As the shear stress on a perfect bicrystal is increased to the theoretical shear strength of the grain boundary, the boundary will undergo a discontinuous change in which some atomic bonds are broken and new atomic bonds are formed. In this manner the grain boundary can slide over distances of many lattice constants.

An alternative approach to the study of grain boundary sliding is to calculate a gamma surface for the boundary. In general this requires some approach other than bicrystal shearing. In bicrystal shearing, a large discontinuous change in the grain boundary offset often occurs as the theoretical shear strength of the boundary is reached. Since the gamma surface plots the energy as a function of offset, such discontinuous change in the offset is undesirable. A further practical difficulty involves precisely defining and calculating the (possibly large) bulk strain energy and subtracting it from the total energy to accurately obtain the gamma surface energy. For these reasons some other method of calculating the gamma surface is desirable.

In this paper we wish to emphasize the relationship between the calculation of gamma surfaces and current research in transition state finding. For details regarding a variety of methods used for transition state finding as well as a comparison of these methods we refer the reader to a recent review.[8] In this paper we will consider two common methods for transition state finding, the "drag" method and the nudged-elastic-band (NEB) method. We first discuss the “drag” method since bicrystal shearing calculations and calculation of gamma surfaces by rigid translation of the two halves of a bicrystal are special cases of the drag method.

The drag method starts with an initial state relaxed to a local energy minimum. Based on some hypothesis regarding the path from this initial state through a transition state to a final state, a reaction coordinate is chosen. This reaction coordinate may be as simple as the x coordinate of a single atom, or may be a generalized reaction coordinate involving simultaneous motions of many atoms. Starting from the initial state, the reaction coordinate is incremented and fixed and the remaining coordinates of the system are allowed to relax. One hopes that this quasistatic calculation will allow the system to evolve smoothly from the initial state to the final state. For simple systems the drag method sometimes works perfectly and is very computationally efficient. However the drag method fails to find the correct transition state in many practical problems. One common mode of failure is directly analogous what happens in a typical bicrystal shearing calculation. The drag method frequently fails because as the reaction coordinate is incremented, the system "snaps" discontinuously from one side of the transition state to the other side of the transition state. In such cases, a plot of energy vs. reaction coordinate shows sharp drops in the energy as the reaction coordinate is increased. Several of the bicrystal shearing calculations in references 4 and 5 show such discontinuous changes in energy. These discontinuous changes in energy will occur during grain boundary sliding, however they are not part of the gamma surface. The magnitude of these discontinuous energy changes are likely to depend on computational factors such as the assumed mechanism for energy dissipation during sliding and the physical size of the two grains.

The drag method can also fail by finding the "wrong" transition state. (By "wrong" we mean a transition state with an activation energy substantially higher than the transition state with the lowest activation energy). This will occur if an incorrect final state is chosen or if the assumed path from the initial state to the final state is wrong. A historic example of this problem is the case of adatom diffusion on a (100) surface[9] (see figure 2-2). Originally, it was assumed that the adatom hopped across the surface moving from one fourfold hollow site to another fourfold hollow site. Later, experimental and theoretical work proved that adatom diffusion on certain (100) surfaces involved the original adatom being incorporated into the surface while one of the surface atoms moved outward to become a new adatom. By this exchange process the adatom in the final state was found in a different fourfold hollow site than the adatom in the initial state.

Similar problems can occur in grain boundary sliding and gamma surface calculations. For example, recent work on grain boundary slippage[10] calculates a gamma surface by rigidly translating the atomic coordinates of all atoms on one side of the grain boundary, constraining all atoms in the directions parallel to the interface, and then relaxing the perpendicular components of all the atomic coordinates to a constrained energy minimum. Actually this is another example of calculating a transition state using the drag method. Here the assumption regarding the transition state is that the two grains translate rigidly past each other. The problem is that this assumption ignores possible complex cooperative motions at the grain boundary. The implicit assumption is that all of the atoms on one side of the boundary maintain their spatial relationship during grain boundary sliding. However the existence of complex cooperative atomic motions has been well documented in a number of computations.[4,11,12,13] Furthermore, the commonly observed phenomena of grain boundary migration perpendicular to the boundary during sliding[7] cannot occur if all of atoms on one side of the boundary move rigidly together as the grain boundary slides. Grain boundary migration requires that atoms start on one side of the grain boundary and move to the other side of the grain boundary during sliding.

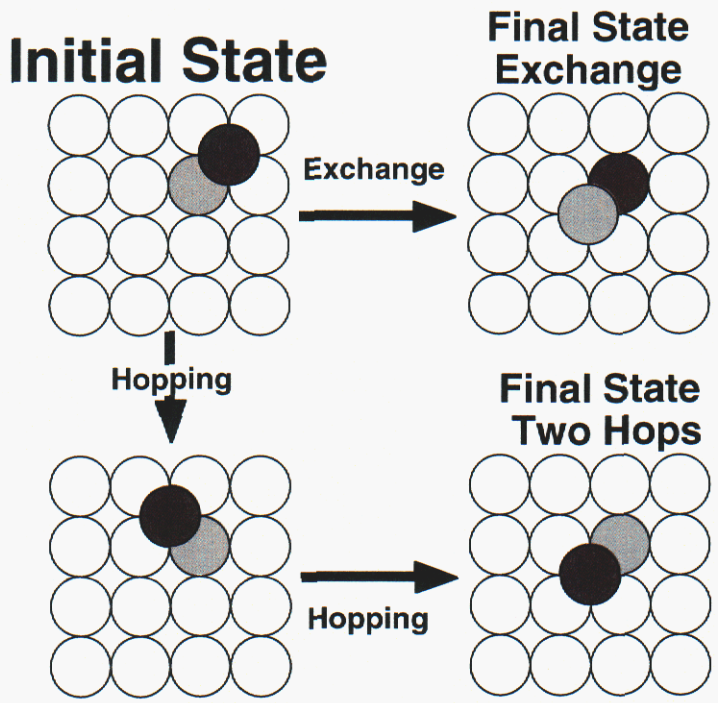

Figure 2-2: Two different mechanisms for surface diffusion on a 100 surface. In the hopping mechanism the black adatom hops across the surface. In the exchange mechanism the black adatom is incorporated in the surface and the gray surface atom moves out of the surface to become an adatom. The final state after two hops is indistinguishable from the final state after exchange if the atoms are not labeled. The two final states are distinguishable if the atoms are labeled. The initial and final states for transition state finding by the nudged elastic band method must be labeled. As shown here, the labeling conveys considerable information regarding the reaction path.

Since complex cooperative atomic motions and grain boundary migration often occur during grain boundary sliding, we suggest that such cooperative motions (if they occur) should be included in a useful definition of the gamma surface for grain boundaries. To avoid possible confusion with the customary definition of a gamma surface, we propose the term generalized gamma surface (GGS) for such cases. We now turn to the question of how to calculate relevant cross-sections of the GGS for a grain boundary.

Drawing upon recent research in transition state finding, we will consider the nudged elastic band method.[14] In order to explain this method, it is convenient to consider the problem of adatom diffusion on a (100) surface once again. Figure 2-2 shows two different final states, one reached by two hopping events, the other reached by a single exchange event. With the atoms labeled, these final states are clearly different. Without the labels, these final states are indistinguishable. The labeling conveys information regarding the reaction pathway. For the nudged elastic band method, labeled initial and final states must be known. A set of n states intermediate between the initial and final state are used for the NEB. Often these states are chosen by linear interpolation between the initial and final states. A fictitious energy is calculated by summing the energy of the n intermediate states plus a term which becomes larger as the difference between adjacent intermediate states increases. Often this term takes the form of a spring potential, thus the term elastic band. The method is refined by adjusting certain components of the forces in order to aid convergence (hence the term nudged) and the fictitious energy is minimized. This gives a set of states and energies along the transition path. The NEB avoids the discontinuous change in energy commonly occurring with drag methods. As should be clear from figure 2-2, it is essential to have properly chosen and labeled initial and final states in order to use the NEB. The NEB has several important advantages for the calculation of grain boundary GGS cross sections. The calculated intermediate states are free of long-range bulk strain. Thus there is no need to attempt to subtract the strain energy of the grains from the total energy in order to obtain the GGS. The NEB also avoids the discontinuities in energy associated with snapping from one configuration to another, often observed in transition state calculations using the drag method.

In order to illustrate many of the issues discussed above, we now consider a specific example, the Al $\Sigma 3$ $(11\bar{2})$ twin boundary. This boundary has been studied extensively using experimental [15.16.17.18] and theoretical methods.[15,17,19] TEM measurements, pair potentials, semiempirical potentials of the embedded atom form, and first principles calculations show that the (111) crystal planes on the two sides of this grain boundary are offset by about ±0.7 Å. The notation, "±", is used here to indicate that there are two degenerate stable configurations, which are symmetry equivalent, but have equal but opposite offsets (see figure 2-3a and 2-3b).

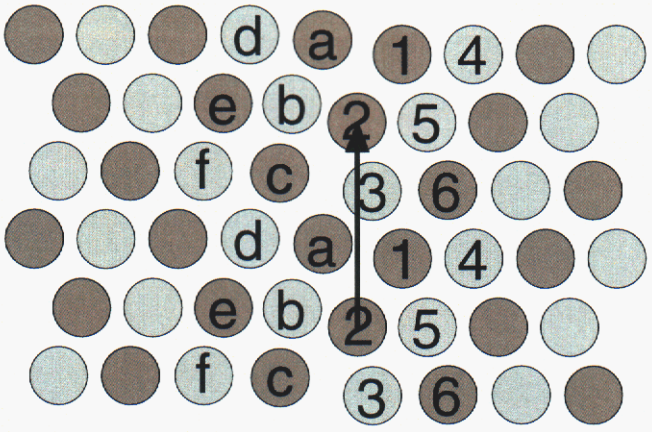

Figure 2-3a: Initial stable configuration of the AlΣ3 ($11\bar{2}$) grain boundary. The atoms on the right hand side of the boundary are labeled with numbers, the atoms on the left hand side of the boundary are labeled with letters (the boundary is defined here by the offset of the 111 planes.) The gray scale indicates position perpendicular to the plane of the paper with lighter atoms being closer to the reader. The arrow in the figure shows the rigid translation of the right hand grain corresponding to a standard gamma surface calculation. This translation is unphysical since there is a very large steric barrier to move atom "2" past atom "a". The actual mechanism of sliding is shown by the other portions of this figure.

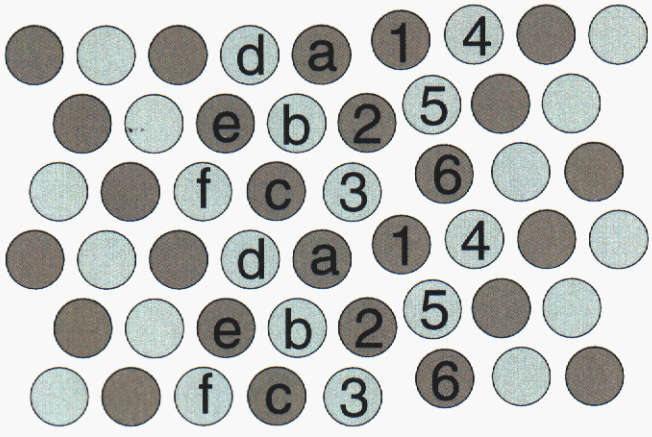

Figure 2-3b: The next stable configuration of the AlΣ3 ($11\bar{2}$) grain boundary. The process of grain boundary sliding involves breaking the bond between atoms "5" and "3" and making a bond between atoms "2" and "6". As a result of this sliding, atoms "2" and "3" move to the left side of the grain boundary.

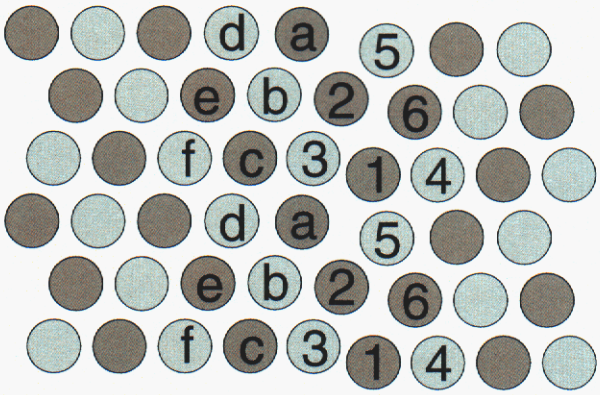

Figure 2-3c: The next stable configuration of the boundary. In sliding from the configuration shown in figure 2-3b to this configuration, a bond is formed between atoms "a" and "5". Grain boundary sliding causes migration of the grain boundary to the right. Since the grain boundary in figure 2-3c is equivalent (with a translation operation) to that in figure 2-3a, further sliding will result in further transfer of atoms across the grain boundary and further grain boundary migration to the right.

It is instructive first to consider the initial and final atomic configurations corresponding to a calculation of the standard gamma surface using the standard approach (i.e. rigid translation parallel to the grain boundary with relaxation perpendicular to the grain boundary). Both the initial and final states are represented by figure 2-3a. The vertical arrow indicates the path for rigid displacement of all of the numbered atoms by a coincidence site lattice (CSL) vector parallel to the boundary. Since this is the size of the unit cell in our calculations, the rigid displacement carries each atom on the right hand side to its image in the next unit cell. We have examined this kind of translation using semiempirical embedded atom calculations. The calculated barrier for this type of grain boundary sliding is extremely large due to the steric hindrance involved in moving atoms "2" and "a" past each other. Such a calculation is irrelevant to grain boundary sliding, because it assumes incorrect atomic motions and associated bond breaking and formation during sliding.

The atomic configurations as a function of offset needed to calculate the GGS will be those that carry the system between two stable configurations with a relatively low activation energy. Finding the atomic configurations at saddles on the energy surface is the goal of transition-state-finding techniques. To use the NEB, labeled initial and final states are required. To obtain this information, we started with a stable initial state shown in figure 2-3a. We used bicrystal shearing (drag) to identify the atomic motions associated with grain boundary sliding, with the assumption that this procedure would allow correcting labeling of the atoms in the final state. Figure 2-3b shows the atomic identifications for a final state (offset +0.7Å) relative to the initial state (offset -0.7Å) shown in figure 2-3a. Figure 2-3c shows the atomic identifications for the next stable state (with offset +1.64Å). We believe the initial and final configurations to be correct because the calculated energy barriers were very small, the atomic pathways from embedded atom and first-principles drag calculations were virtually identical, and structures similar to those calculated here have been observed in TEM microphotographs of partial grain boundary dislocations at this boundary.[20]

The process of sliding this grain boundary involves complex cooperative motions of the atoms in the vicinity of the grain boundary as shown in figure 2-3. While bicrystal shearing can provide a guide to the cooperative motions likely to occur, it is not a good way to calculate the generalized gamma surface. Instead we obtained cross sections of the GGS by using first principles calculations with the nudged elastic band method. We used the plane wave (E_{cut}= 250 eV) and ultrasoft pseudopotential[21] based code, VASP, developed by Kresse and Furthmuller.[22] The unit cell was a slab containing 48 atoms. The k-point sampling for the final calculations was 40x3x18; Methfessel/Paxton smearing[23] of order 1 with a smearing width of 0.15eV was used. The effect of the energy cutoff, the k-point sampling, the use of the LDA and the GGA approximation, the smearing width, and number of states for the NEB were all investigated. Based on these tests, we believe that our calculated barriers for grain boundary sliding are correct within ±2mJ/m^2.

Figure 2-4 shows the energy curve calculated by the elastic band method described above. The stable states at -0.7Å offset, 0.7Å offset, and 1.64Å offset correspond to the three atomic configurations shown in Figure 2-3a, 2-3b, and 2-3c respectively. The transition state at 0.0Å has the (111) planes on both sides of the grain boundary aligned, hence the term symmetric. The transition state at 1.17Å has the (111) planes on the right side of the boundary halfway between the (111) planes on the left side of the boundary, hence the term anti-symmetric. The maximum derivative of this curve gives the theoretical shear strength of this grain boundary. By theoretical we mean the shear strength of an ideal boundary without any dislocations. For this boundary the calculated theoretical shear strength is 0.28 GPa. This is considerably less than the calculated theoretical shear strength of a perfect Al crystal in the $[11\bar{2}]$direction on a (111) plane given as 1.85 GPa by Roundy et. al.[6] Using elasticity theory with the published elastic constants of aluminum, the theoretical shear strength of the Al Σ 3 $(11\bar{2})$ grain boundary will be reached at an engineering shear strain of 0.014 for the bulk aluminum grains comprising the bicrystal shown in figure 2-1.

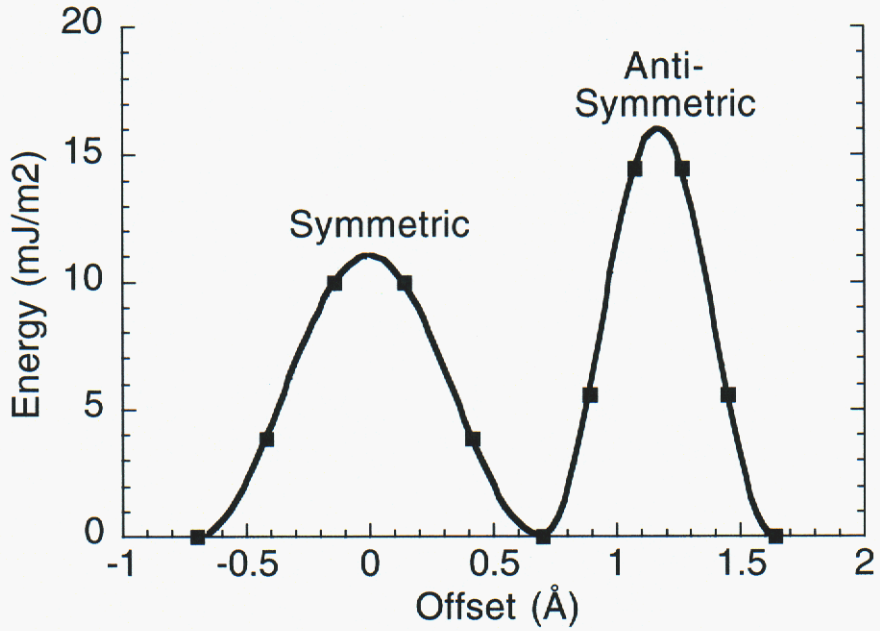

Figure 2-4: Energy per unit area as a function of planar offset for AlΣ3 $(11\bar{2})$ grain boundary. Energies were determined using nudged elastic band first principles calculation as described in text. The relevant stable configurations are shown in figure 3. The transition state configurations are labeled symmetric for the state having the (111) planes on both sides of the grain boundary aligned and antisymmetic for the state having the (111) planes on one side of the grain boundary halfway between the (111) planes on the other side of the boundary. The maximum derivative of this curve (found at about 0.94Å offset) corresponds to the theoretical shear strength of this grain boundary.

In conclusion we present the following picture of grain boundary sliding. We propose that the concept of the gamma surface should be retained, but that the definition of the gamma surface must be considered carefully for a given grain boundary since complex cooperative atomic motions may occur during sliding. In order to avoid confusion we suggest that the gamma surface incorporating cooperative atomic motions be called the generalized gamma surface (GGS). Once the GGS is calculated, the maximum gradient of this surface along a transition path corresponds to the theoretical shear strength of a grain boundary in that direction. Bulk elasticity can be used to determine the bulk strain associated with this shear strength. Below this bulk strain, the two perfect grains will undergo a shear strain and displacements at the grain boundary will be only a fraction of a lattice spacing (i.e. no grain boundary sliding). At and above this bulk strain, grain boundary sliding will occur. Grain boundary sliding is likely to involve atomic motions similar to those comprising the GGS, but because of the energy release and dissipation which will occur in a discontinuous fashion at the boundary it will be relatively difficult to model. Finally, realistic calculations will need to consider the important role that grain boundary dislocations must play in grain boundary sliding. Although semiempirical calculations using the nudged elastic band method have been performed to address the issue of dislocation motion at grain boundaries first principles calculations of these phenomena remain well beyond our present computational capabilities. Hopefully it will be possible to use the GGS as defined and calculated here to model grain boundary dislocations and to better understand the role of grain boundary dislocations in allowing grain boundary sliding in real materials.

Finally, we should mention that some calculations of grain boundary sliding in semiconductors have shown permanent damage propagating from the interface.[5] If permanent damage occurs during sliding, the generalized gamma surface would not be a appropriate way to model the sliding process. The concept of a gamma surface is only useful if an interface reforms its original structure periodically during sliding.

References

1 V. Vitek, Phil Mag **18**, 773 (1968).
2 A. P. Sutton and R. W. Balluffi, "Interfaces in Crystalline Materials", Clarendon Press, Oxford, (1996). See sections 12.8.1.1 and 2.11.2.1.
3 J. Hartford et. al., Phys. Rev. **B 58**, 2487 (1998).
4 C. Molteni et. al., Phys. Rev. Lett. **79**, 869 (1997).
5 C. Molteni et. al., Phys. Rev. Lett. **76**, 1284 (1996).
6 D. Roundy et. al., Phys. Rev. Lett. **82**, 2713 (1999).
7 M. Winning et. al., Acta. Mater. **49**, 211 (2001).
8 G. Henkelman, G. Jóhannesson, and H. Jónsson, in "Progress on Theoretical Chemistry and Physics", edited by S. D. Schwartz, Kluwar Academic Publishers, 2000.
9 G.L. Kellogg and P.J. Feibelman, Phys. Rev. Lett. **64**, 3143 (1990).
10 M.D. Starostenkov et. al., Comp. Mat. Sci. **14**, 146 (1999)
11 G.H. Bishop et. al., in "Grain Boundary Structure and Kinetics" pp. 373-377, American Society for Metals, Metals Park Ohio, 1980.
12 R. J. Kurtz, R. G. Hoagland and J. P. Hirth, Phil. Mag. A, **79**, 665 (1999).
13 The calculation for AlΣ3 $(11\bar{2})$ reported here also shows such cooperative atomic motions.
14 H. Jónsson, G. Mills, and K. W. Jacobsen, in "Classical and Quantum Dynamics in Condensed Phase Simulation's", edited by B. J. Berne, G. Ciccotti, and D. F. Coker, World Scientific, Singapore, 1998.
15 R. C. Pond and V. Vitek, Proc. R. Soc. London Ser. **A 357**, 453 (1977).
16 R. C. Pond, Proc. R. Soc. London Ser. **A 357**, 471 (1977).
17 D. L. Medlin et. al., Mat. Res. Soc. Symp. Proc. **295**, 91 (1993).
18 B. J. Inkson, R. Spolenak and T. Wagner, Inst. Phys. Conf. Ser. No. **161**, 335 (1999).
19 A.F. Wright and S.R.Atlas, Phys. Rev. B **50**, 15248 (1994).
20 D.L. Medlin et. al., Phil. Mag. A 75, 733 (1997).
21 D. Vanderbilt, Phys. Rev. B **41**, 7892 (1990).
22 G. Kresse and J. Furthmuller, Phys. Rev. B **54**, 11169 (1996).
23 M. Methfessel and A. T. Paxton, Phys. Rev. B **40**, 3616 (1989).

This page intentionally left blank

III. Determination of Facet Size for Aluminum Grain Boundaries

High-energy grain boundaries (GBs) commonly undergo faceting to reduce their total energy. In many cases, the facets are observed to have uniform finite lengths, and the GB shows a sawtooth profile [1]. This self-organization of GB facets is important in determining mechanical properties of polycrystalline materials and in understanding the mechanisms of GB defaceting.

A particularly well-studied GB is the aluminum twin boundary with average $[1\,\bar{1}\,0]$ orientation, which separates two grains related to each other by a 180° rotation about a shared [111] axis. The faceting of this GB has been previously studied experimentally using transmission electron microscopy (TEM) [2]. At room temperature, this boundary spontaneously facets into regular $\Sigma 3\{112\}$ type facets with lengths of about 100 nm.

The equilibrium theory commonly invoked [1] to explain the finite facets is based on the premise that there exists a balance between attractive and repulsive forces between facet junctions. This is similar to the theory of stress domains on surfaces [3], where the energy cost of forming facet junctions is balanced by strain energy relief. As discussed below, for the GB, the repulsive force is due to the presence of dislocations at the facet junctions while the attractive force is due to GB stress. [We emphasize that GB stress is an interfacial stress (units of force/distance) not a bulk stress (units of force/area)].

There appear to be two reasons why a quantitative validation of the accepted theoretical explanation is still lacking. Experimentally, there are very few measurements of GB stress. (Recent x-ray diffraction measurements [4] have been used to estimate high-angle GB stress in Pd nanocrystals, but this is not a routine measurement). Theoretically, an explicit analytical expression for the energy of the faceted GB has not yet been presented, and atomistic calculations have not yet been performed to address this issue.

Here we combine continuum elasticity theory, density functional theory (DFT), and embedded-atom method (EAM) calculations to show that the conventional energetic argument cannot possibly account for the experimental observations of finite facet lengths for the above aluminum GB with average $[1\,\bar{1}\,0]$ orientation. To do this, we first use continuum elasticity calculations to show that stabilization of finite facets arises when the GB stress exceeds a threshold value; for stresses below the threshold value, the energy is minimized by facets of infinite length. Using DFT and EAM, we show that the actual stress for the aluminum GB is much smaller than the threshold value, causing the equilibrium facet length to tend to infinity. Finally, this is confirmed by EAM calculations of the total energy as a function of facet length for the aluminum bicrystal with multiple GB facets.

We begin by discussing a planar GB to establish the key concepts of translation vector and GB stress. In general, GBs are characterized by a lower atomic density, which alters the equilibrium bond lengths compared to the bulk and induces a discontinuity in the spacing of lattice planes at the GB.

The subset of lattice points forming a nearly continuous lattice across the GB is known as the coincident site lattice (CSL); the translation vector t measures the discontinuity in the CSL at the GB [5]. The lower atomic density at the GB also changes equilibrium bond lengths in the plane of the GB; however, this relaxation is only partial because of the coupling to the bulk lattice. Hence, the GB is in a state of stress [1], with a constant stress tensor component τ in the GB plane.

This description of the GB in terms of a translation vector and interfacial stress allows us to develop a simplified model of the faceted GB that is amenable to continuum elasticity calculations. Figure 3-1 shows a schematic of the faceted GB. When two GBs meet at an angle to form a facet junction, the translation vectors on the right, t_{right}, and on the left, t_{left}, are different, leading to a Burger's vector $b = t_{right} - t_{left}$ at the facet junction [5]. At a junction between two facets, there is also a discontinuity of the stress tensor, leading to a line force $\mathbf{p}^n = \pm 2\tau \sin\phi\,\delta(x - x_n)\delta(y - y_n)\mathbf{j}$, where (x_n, y_n) is the position of the facet junction, ϕ is the GB angle, and the top (bottom) sign corresponds to a valley (crest). With this model of the faceted GB, we can now calculate its energy as a function of facet length L using isotropic continuum elasticity.

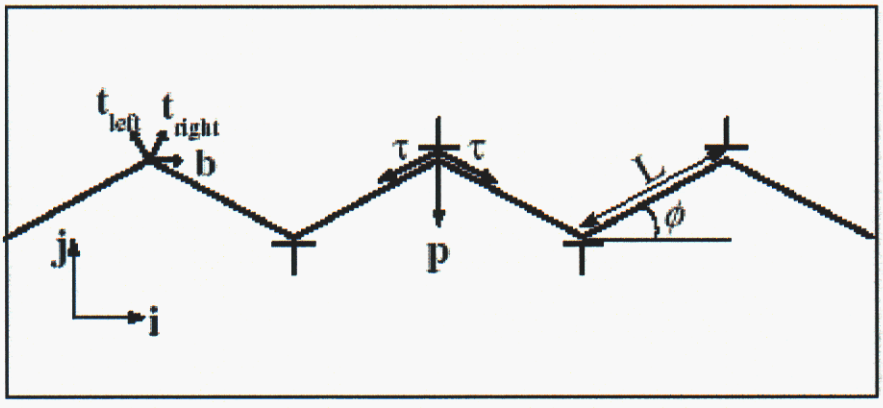

Figure 3-1: Sketch of the GB used for the continuum elasticity calculations.

The energy of the GB per unit area can be written as $E = E_{d\text{-}d} - E_{lf\text{-}lf} - E_{d\text{-}lf}$ where $E_{d\text{-}d}$ is the interaction energy between the dislocations, $E_{lf\text{-}lf}$ is the interaction energy between the line forces, and $E_{d\text{-}lf}$ is the interaction energy between the dislocations and the line forces (all of which include self-interactions). The three components of the energy can be calculated from

$E_{\alpha-\beta} = -\frac{1}{2A}\sum_{m,n}\int f_i^{m\alpha}(\mathbf{r})u_i^{n\beta}(\mathbf{r})$ where α,β=d or lf, repeated indices imply summation, and A is the area of the unfaceted GB. Here, $f_i^{m\alpha}(\mathbf{r})$ and $u_i^{m\alpha}(\mathbf{r})$are the force and elastic displacement caused by the mth dislocation or line force, in the i = x, y or z direction. The displacements $u_i^{md}(\mathbf{r})$are given in standard elasticity references [6] while $u_i^{mlf}(\mathbf{r})$can be calculated from

$u_i^{mlf}(\mathbf{r}) = \int G_{il}(r-r')p_i^m(r')$

where $G_{il}(r)$ is the Green's function for an infinite isotropic elastic medium [6].
From the expressions above, we find that the energy is of the form E(L) =(A/L) lnL + B/L with

$$A = \frac{b^2\mu^2 - 2(3-4\sigma)(1+\sigma)\tau^2\sin^2\phi + 4\tau b\mu\sin\phi(1-2\sigma)}{4\pi\mu(1-\sigma)\cos\phi}$$

and B is a constant that is unimportant for our purposes. Here σ is the Poisson ratio and μ is the shear modulus. From the functional form E(L) =(A/L) lnL + B/L, one can show that finite facets will be stabilized when A<0, leading to the condition

$$\tau > \frac{b\mu(1-2\sigma+\sqrt{7-6\sigma-4\sigma^2}}{2(1+\sigma)(3-4\sigma)\sin\phi} = \tau^*$$

Hence, for finite facet lengths to be energetically favorable, the GB stress must exceed a threshold value τ^*.

Based on the above theory, the conventional explanation for the finite facet size observed at the Al twin boundary with average $[1\bar{1}0]$ orientation is that the GB stress τ is larger than τ^*. However, no experimental or theoretical values for τ or τ^* are available for this GB, making validation of the conventional model difficult.

In order to investigate this issue, we used DFT and EAM to calculate τ and τ^* for an Al $\Sigma3$ $(1\bar{2}1)$ twin boundary. Our basic approach to obtain τ is to use a planar GB representing a facet and calculate the stress of this GB. To obtain τ^*, we calculate the translation vector t of this GB, obtain b $= t_{right} - t_{left}$ and substitute in the equation above. We used a bulk slab with a small rectangular cross section and a long length in the $[1\bar{2}1]$ crystallographic direction. Periodic boundary conditions were used in all three directions. In order to ensure a completely stress-free bulk slab, the periodic lengths were relaxed in all three directions. Next, two equally spaced GBs were introduced with normals in the long $[1\bar{2}1]$ direction, as shown in Fig. 3-2. The slab periodic length, $L_{1\bar{2}1}$, in the direction normal to the GBs was then relaxed to allow for the excess volume of the GBs and the differing atomic density in the vicinity of the GBs. The translational vector t was calculated from the new periodic length in this long direction. Finally, we found the desired component of the GB stress by calculating the total system energy as a function of the appropriate periodic length, L_{101}, of the GB plane, while holding the other two periodic lengths fixed. A more complete description of these calculations follows. Voter-Chen potentials for aluminum were used for the EAM calculations [7]. Our density-functional [8,9] calculations

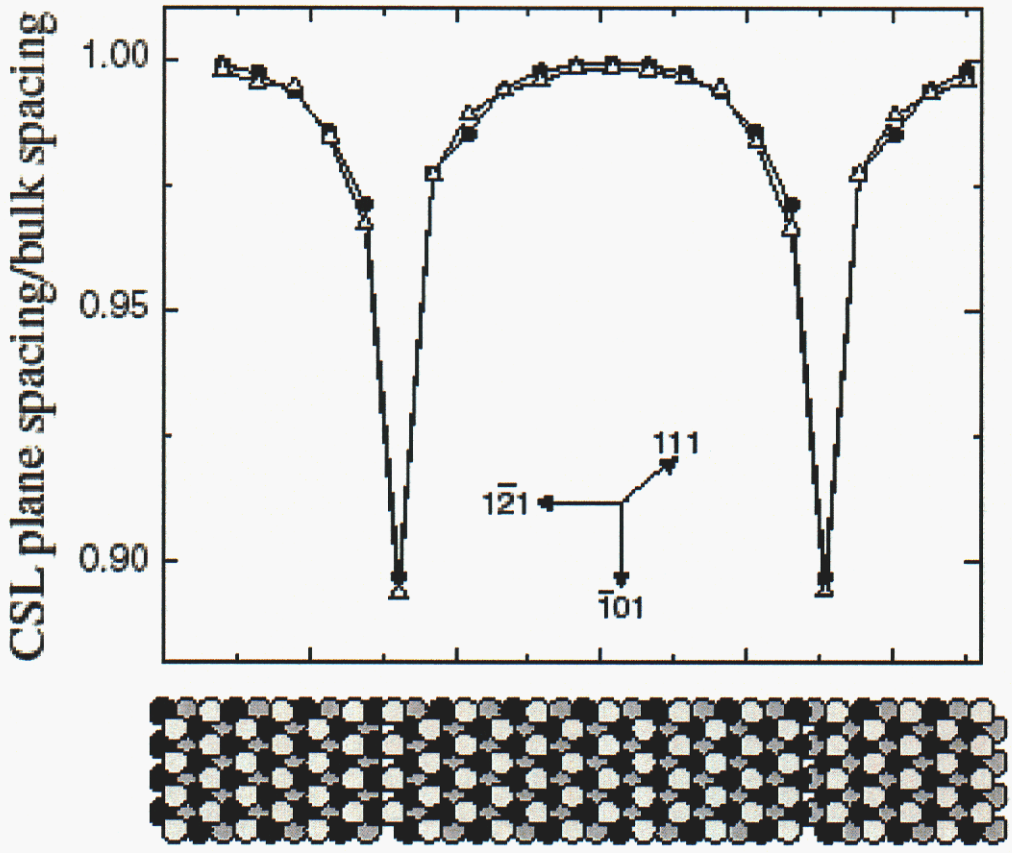

Figure 3-2: Spacing of (121) CSL planes in Al with two (121) twin boundaries calculated from DFT (open traingles) and EAM (solid circles). Simulation supercell (replicated four times in the [101] direction) is shown below the figure, with black circles representing atoms forming the CSL.

were performed with theVienna ab initio simulation package (VASP) [10], which uses a plane-wave basis for expansion of the electronic wave functions combined with the generalized gradient approximation [11] for the exchange-correlation energy. Ultrasoft pseudopotentials [12,13], including partial core corrections [14], were used to model the computationally expensive core-valence interaction. Brillouin zone sampling was performed using a Monkhorst-Pack grid [15], and electronic occupancies were determined according to a Methfessel-Paxton scheme [16] with an energy smearing of 0.15 eV. The number of k points was chosen to ensure that the elastic constants were converged to within 10% of the experimental values for bulk Al. This required the use of a very dense k grid (40 x 20 x 2), resulting in 400 irreducible k points. The plane-wave cutoff energy was set to 180 eV, which was sufficient to converge total energies to within 1–2 meV/atom.

For our DFT calculations, we started with a 72 atom GB-free bulk Al slab with periodic lengths L_{101}, L_{111}, and L_{121} in the three orthogonal slab directions. After careful relaxation of these periodic lengths to better than 0.1% tolerance, we found L_{101} =2.864 Å , L_{111} = 7.005 Å , and L_{121} = 59.376 Å . In order to form two GBs, the central section of the unit cell was subjected to a reflection operation about a [111] mirror plane and two atoms were removed to create a 70-atom slab (shown relaxed and replicated in Fig. 3-2). The lengths L_{101} and L_{111} were fixed at the bulk stress-free values and L_{121} was varied to minimize the total energy, thus allowing for the lower atomic density and the excess volume of the GB. Similar methods were used for the EAM calculations.

Figure 3-2 shows the spacing of the CSL planes in the presence of the GBs. Clearly, the CSL is contracted at the GBs compared to the bulk system; as explained above, the contraction occurs because the atomic density is lower at the GBs, leading to a decrease in the average coordination of each atom and slightly shorter bonds. As Fig. 3-2 clearly shows, we obtain excellent agreement between the DFT and EAM calculations, with a total contraction of the simulation cell in the (121) direction of 0.54 Å per GB for DFT and 0.51 Å for EAM [17]. Thus, taking the DFT result, the magnitude of the Burger's vector that enters in Eq. (5) is 0.54 Å . Our calculations are in good agreement with experiment [5] and previous calculations [5,18,19].

With this value for the Burger's vector and published values for the elastic constants of aluminum [20], we find from the above equation that, for this particular GB, τ^*=99 meV/Å^2. The remaining question is whether the actual stress τ is above or below this value. For the calculation of the GB stress, we used the slab from the previous calculation (shown in Fig. 3-2). L_{111} and L_{121} were fixed at their bulk stress-free values and the total energy was calculated as a function of L_{101}. The result of this calculation is plotted in Fig. 3-3, where the energy reference has been adjusted so the minimum of energy is at zero. As can be seen in the figure, the energy minimum is displaced from the bulk stress-free value because the GB stress has the effect of contracting the slab slightly in the [101] direction. The GB stress is given by

$$\tau = \frac{1}{2L_{111}} \frac{\partial E}{\partial L_{101}}\bigg|_{L_{101}=2.864\,A}$$

(The partial derivative is evaluated at the periodic length of the stress-free bulk slab). Using this method, we calculate a grain boundary stress of 21 = meV/Å^2 using DFT and 29 meV/Å^2 using EAM. Given the uncertainties in the DFT and EAM calculations, these values agree within anticipated errors. The important point here is that both of these stresses are much smaller than the value τ^*=99 meV/Å^2 calculated above. This large difference between the actual stress τ and the threshold stress τ^* can be further highlighted by comparing the DFT and EAM curves of Fig. 3-3 with a continuum elasticity calculation for a slab with two GBs having the threshold stress τ^*=99 meV/Å^2. Within continuum elasticity, the energy to deform the bulk slab (without the GB) is

$$E_{bulk} = \frac{V_o}{4}(C_{11} + C_{12} + 2C_{44})\left(\frac{\partial L_{101}}{L_{101}}\right)^2;$$

where V_o is the undeformed slab volume and the C_{ij} are the elastic constants. . Adding the two GBs costs an additional energy, $E_{GB} = 2L_{111}\tau^*\Delta L_{101}$ The energy $E_{bulk} + E_{GB}$ is plotted as a dotted line in Fig. 3-3.

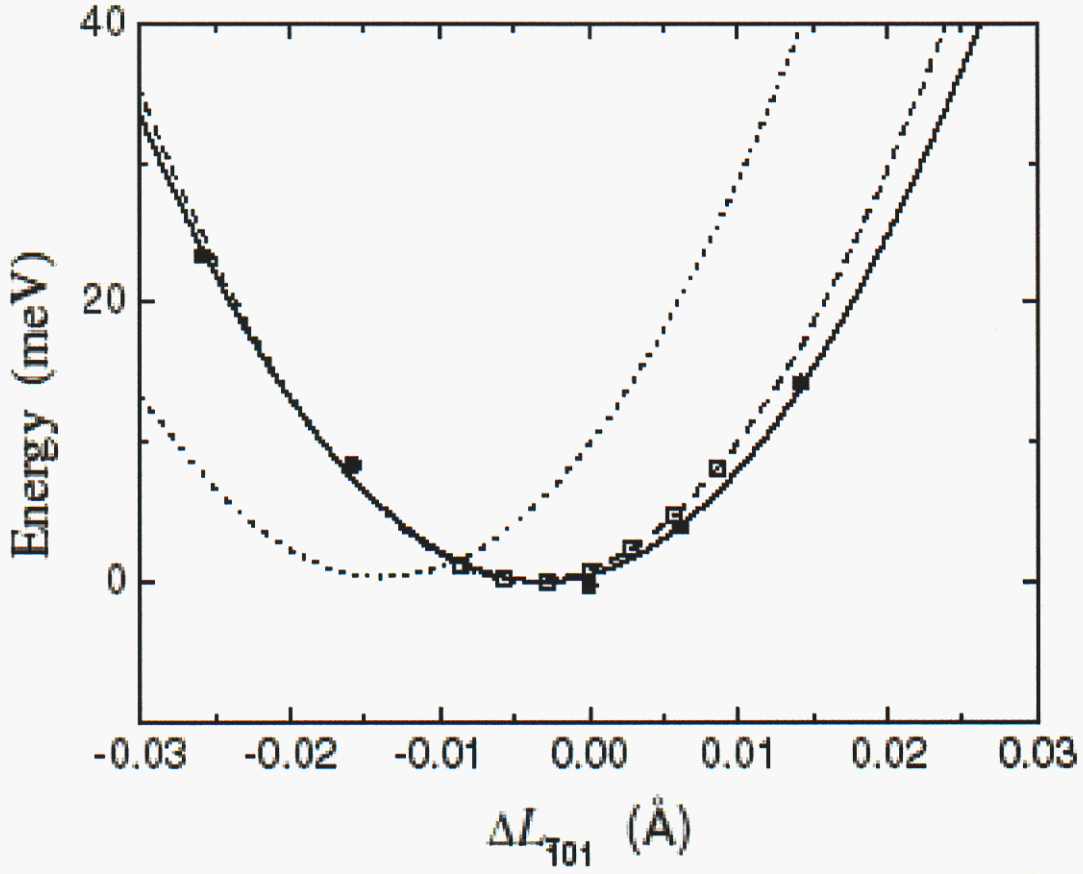

Figure 3-3: Energy of the grain boundary of figure 3-2 as a function of the change in L_{101} from its bulk stress-free value, calculated from DFT (solid circles) and EAM (open squares). The solid and dashed lines are quadratic fits. The dotted line is the energy calculated from continuum elasticity using a GB stress of τ^*.

Comparison of the DFT, EAM, and continuum elasticity curves shows agreement in the curvature, demonstrating that the atomistic calculations give the correct values for the bulk elastic constants. More importantly, the slope of the atomistic curves and the continuum elasticity curve are very different at $\Delta L_{101} = 0$. This reemphasizes that τ calculated from the atomistic calculations is much smaller than τ^*, demonstrating clearly that finite facets are not stabilized by GB stress at this grain boundary.

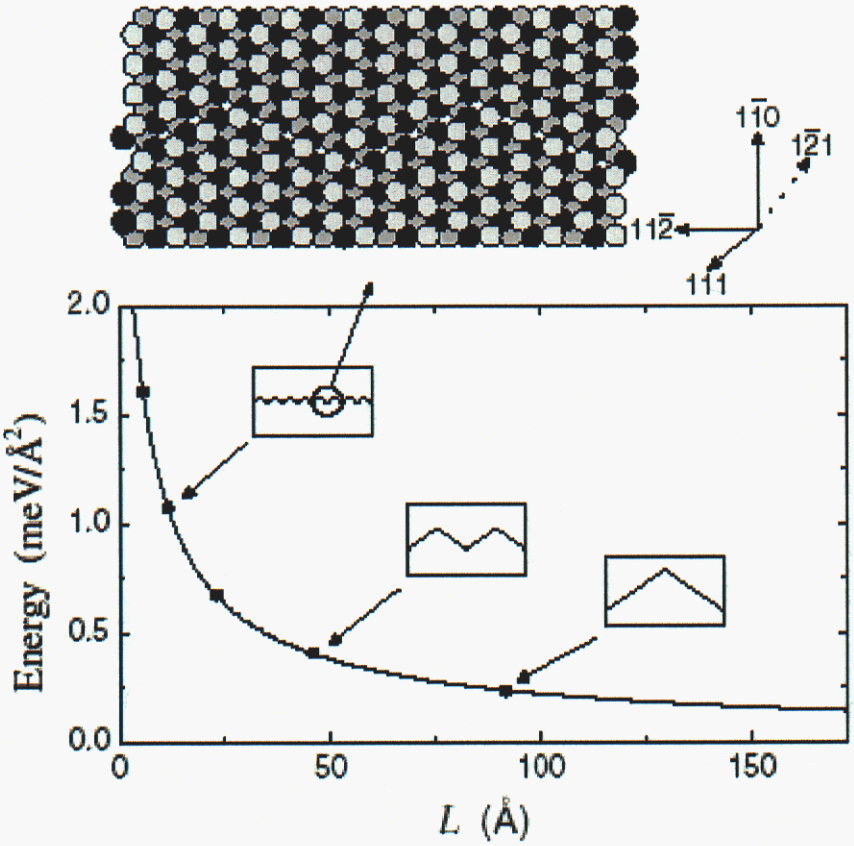

Figure 3-4: :ntation faceted into Σ 3 {112} type boundaries, as a function of facet length. The points are fit by the function (A/L)lnL+B/L. The insets show schematically the geometries used for some of the calculated points.

This conclusion can be directly verified by EAM calculations of the energy of a faceted Al boundary as a function of facet size using a geometry that replicates the experimental TEM observations. Figure 3-4 shows a schematic representation of a portion of this geometry. We modeled a 397 Å thick slab with two free [110] surfaces and a single GB with average [110] orientation in the center. The periodic boundary lengths in the [111] and [112] directions were 7.01 and 158.7 Å , respectively. Thfese boundary conditions were selected to allow modeling fairly long facets while avoiding interference of the GB strain field with the slab surface. For this bicrystal, we calculated the total relaxed energy with n facets of length 183.3 Å /n (n _ 2, 4, 8, 16, and 32). All of these configurations contained the same number of atoms, the same area of free surface, and the same total GB area; thus, the changes in total energy directly reflect the GB energy as a function of facet length. Figure 3-4 shows the calculated energy as a function of facet length L. The plotted points are well fit by a curve of the form (A/L) ln_L+ B/L. Least squares fitting to the total EAM energies gives A = 4.96 meV/Å^2 and B meV/Å^2. Since A is positive, there is no local minimum in the energy and no finite equilibrium facet length. The curve fit confirms what the plotted points suggest: The equilibrium GB facet length for the EAM calculation tends toward infinity, confirming the predictions from the continuum elasticity calculation. As a final check of the above calculations and derivation, we can compare the

values of A calculated from the EAM and the prediction from the elasticity calculation. From Eq. (4) and the values for b and τ from EAM, we find A = 6.5 meV= _A in good agreement with the EAM result A = 4.96 meV/Å^2. This is a strong check of the EAM calculations and of the continuum elasticity derivation. The work presented here shows that finite facets are not equilibrium features of this GB.While the obvious alternative is kinetics, the actual atomistic kinetic mechanism remains to be explored, as does the generalization of the conclusion to other GBs.

References

[1] A. P. Sutton and R.W. Balluffi, Interfaces in Crystalline Materials (Oxford University Press, New York, 1996).

[2] T. E. Hsieh and R.W. Balluffi, Acta Metall. 37, 2133 (1989).

[3] V. I. Marchenko, Sov. Phys. JETP 54, 605 (1981).

[4] R. Birringer, M. Hoffmann, and P. Zimmer, Phys. Rev. Lett. 88, 206104 (2002).

[5] R.C. Pond and V.Vitek, Proc. R. Soc. London, Ser. A 357, 453 (1977). [6] L. D. Landau and E.M. Lifshitz, Theory of Elasticity (Butterworth-Heinemann, Stoneham, MA, 1995) 3rd ed.

[7] A. F. Voter and S. P. Chen, in Characterization of Defects in Materials, edited by R.W. Siegel, J. R.Weertman, and R. Sinclair (Materials Research Society, Pitttsburgh, PA, 1987), pp. 175–180.

[8] P. Hohenberg and W. Kohn, Phys. Rev. 136, B864 (1964).

[9] W. Kohn and L. J. Sham, Phys. Rev. 140, A1133 (1965).

[10] G. Kresse and J. Furthmu¨ller, Phys. Rev. B 54, 11169 (1996).

[11] J. P. Perdew et al., Phys. Rev. B 46, 6671 (1992).

[12] D. Vanderbilt, Phys. Rev. B 41, 7892 (1990).

[13] G. Kresse and J. Hafner, J. Phys. Condens. Matter 6, 8245 (1994).

[14] S.G. Louie, S. Froyen, and M. L. Cohen, Phys. Rev. B 26, 1738 (1982). [15] H. J. Monkhorst and J. D. Pack, Phys. Rev. B 13, 5188 (1976).

[16] M. Methfessel and A.T. Paxton, Phys. Rev. B 40, 3616 (1989).

[17] There is also a CSL shift of 0.7 Å in the [111] direction at the GB. This shift cancels when subtracting the two facet translation vectors to get the Burger's vector for a GB facet junction.

[18] D.C. Medlin et al., MRS Symp. Proc. 295, 91 (1993).

[19] A. F. Wright and S. R. Atlas, Phys. Rev. B 50, 15248 (1994).

[20] J. P. Hirth and J. Lothe, Theory of Dislocations (Krieger, Malabar, FL, 1992), 2nd ed.

This page intentionally left blank

IV. Overlayer Strain Relief on Surfaces with Square Symmetry:

Phase Diagram for 2D Frenkel-Kontorova Model

Virtually every surface, with or without a heteroepitaxial overlayer, is strained. For clean surfaces, the coordination of surface atoms is lower than bulk atoms, thus the surface atoms prefer a different interatomic spacing from the bulk atoms. For overlayers, the lattice constants of the overlayer and the substrate are not perfectly matched. Since the mechanisms of strain relief determine the structure of clean surfaces and overlayers, it is essential to understand these mechanisms in order to predict and control such structures.

In this paper, I consider the structure of overlayers on surfaces with square symmetry. Experimentally a great variety of structures have been observed for overlayers on (100) surfaces. These include pseudomorphic structures, pseudomorphic structures with intersecting rectangular dislocation arrays[1], clock-rotated structures[2], hexagonal overlayers of various periodicities[3] and rotated hexagonal overlayers.[4] More recently, nonintersecting dislocation lines have been observed for Cu deposited on Ni(100).[5] Ideally, one would like to have a single theory which can explain in a systematic manner the wide range of structures observed for overlayer systems on (100) surfaces. This has proved an elusive goal.

There are a number of theoretical approaches that have been applied to this problem. The classic work in this area is by Frank and Van der Merwe (FVM).[6] In their continuum approach they consider the problem as two superimposed one-dimensional problems. Their theory predicts intersecting dislocations forming an approximately square grid. It has been extremely successful in addressing issues of strained layer growth on Si(100) for example. Their theory cannot however treat situations in which a hexagonal film forms on a square substrate. Other work has addressed the reconstruction of fcc metal 100 surfaces, specifically Au, Pt and Ir to form hexagonal overlayers, sometimes rotated with respect to the substrate.[7] Finally there is considerable work using molecular dynamics[8] and/or Monte Carlo techniques[9] to study the structure of films grown on (100) surfaces.

In this paper I consider the phase diagram for a model of an overlayer on a square substrate as a function of the lattice mismatch between substrate and overlayer. The most important feature of this model is that it includes both hexagonal and square symmetry overlayers and the transition between these two symmetries. In contrast to molecular dynamics and Monte Carlo techniques, the energetics of defect free single phases at 0K are calculated and compared. This 2D Frenkel Kontorova model is of fundamental theoretical interest. In addition, the solutions are useful because they suggest phases which should be tested in detailed atomistic calculations of strain relief. As an example of this application, first-principles calculations performed here show that a nickel (100) surface subjected to a strain parallel to the surface reconstructs from a bulk termination to a clock rotation for biaxial compressive strain exceeding 2.4%.
For a 2D Frenkel Kontorova model the adatoms move in a substrate potential:

$$V_{sub}(\vec{r}) = \frac{V_0}{4}\left(\cos\frac{2\pi x}{a} + \cos\frac{2\pi y}{a} + 2\right) \quad .$$

V_0 determines the strength of the substrate potential and a is the lattice constant for the 2D square surface lattice. For the numerical study reported here, V_0 was chosen as 0.8 eV corresponding to a fourfold hollow energy of 0.0 eV, a bridge site energy of 0.4 eV and an on-top site energy of 0.8 eV. These are plausible values for a (100) fcc metal surface. The lattice spacing, a, was set equal to 2.49 Å, the nearest neighbor spacing of bulk nickel.

In a 1D Frenkel-Kontorova model, nearest neighbor atoms are connected by springs. Since the atoms are in a linear chain, each atom has one nearest neighbor on each side. In a 2D Frenkel-Kontorova model, the definition of nearest neighbors can be problematic, and it is customary to avoid ambiguity by using a short range adatom-adatom potential with a binding energy, ε. Leonard Jones and Morse potentials are common choices. In order to facilitate comparison with analytical calculations, including the work of FVM, I chose instead a piecewise continuous function made of two parabolic segments. This potential is shown in figure 1. Over most of its range ($r<r_1$) it has the form $V(r) = -\varepsilon + (k/2)(r-r_o)^2$. The minimum of this potential is at $r = r_o$ and the binding energy is ε. In order to continue this function to zero, it was joined to an inverted parabola for the remainder of its range, $V(r) = -(k/2)(r-r_2)^2$ for ($r_1<r<r_2$). By matching V(r) and its derivative at r_1, the values of r_1 and r_2 are determined. The range of the potential is $r_2 = r_o + 2\sqrt{\varepsilon/k}$.

The value for ε was initially chosen to fit the cohesive energy of nickel and the value of k was chosen based on a Leonard Jones potential with the binding energy and lattice constant of nickel. This choice (ε=0.7eV and k=10eV/Å^2) gave hexagonal overlayers for all values of the overlayer misfit. In order to investigate the competition between pseudomorphic and hexagonal overlayers commonly seem for metal surfaces and overlayers, I chose instead ε = 0.35eV and k=10eV/ Å^2. All of the results reported here were obtained with these parameters.

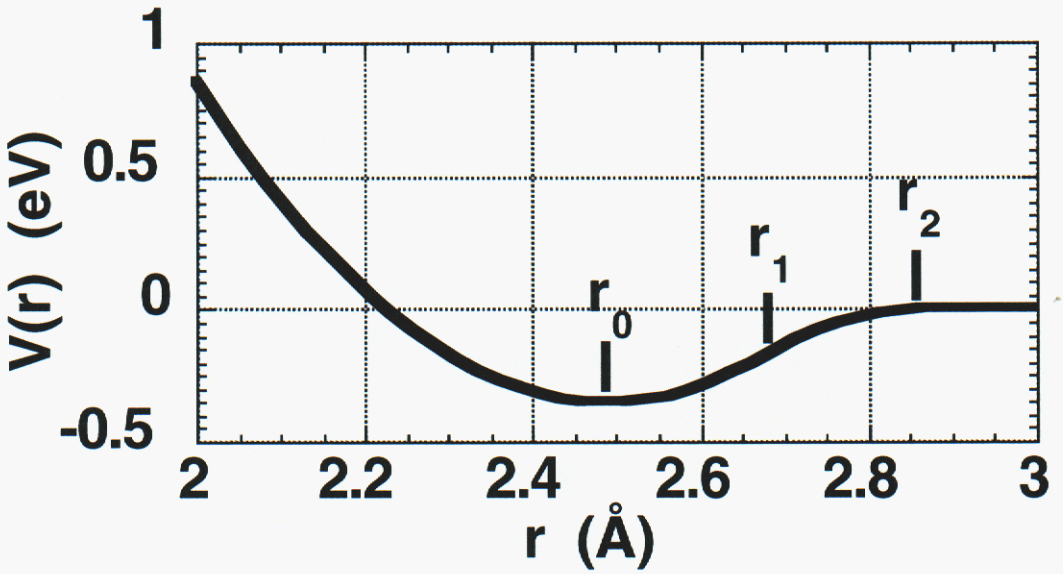

Figure 4-1: Adatom-adatom potential used in these calculations. The potential has a binding energy, ε, a spring constant, k, and is parabolic for $r<r_1$. For $r>r_1$ the potential is an inverted parabola, out to a cutoff radius at r_2.

The total energy of a system of adatoms adsorbed on the surface is the sum of the substrate energy for all of the adatoms, and the adatom energy for all of the adatom-adatom bonds:

$$E_{total} = \sum_j V_{sub}(\vec{r}_j) + \sum_{i \neq j} \sum_j V_{ad}(| \vec{r}_i - \vec{r}_j |)/2$$

The energy per atom, E, is this energy divided by the number of adatoms. In order to construct the zero temperature phase diagram for this model, one must find single phase arrangements of atoms which fill two-dimensional space (with periodic boundary conditions) and which minimize E. I started with a variety of initial atomic configurations (to be described), picked a value of the lattice mismatch, $\Delta = (r_0 - a)/a$, and used the conjugate gradient technique to minimize the total energy as a function of the atomic positions. The calculations were limited to mismatchs in the range $-0.2 < \Delta < 0.2$. Atomic arrangements resulting from the minimization with more than one phase or with defects were rejected. By repeating this procedure for a complete set of reasonable initial trial configurations, the global minimum energy configuration was found for various values of the mismatch, Δ. In practice, the key issue was to identify a complete set of reasonable initial trial configurations. It was hard to be sure that this set was complete. I was guided in this task by experimental results showing configurations with fourfold coordination to other adatoms (rectangular packing) and configurations with sixfold coordination to other adatoms (hexagonal packing). These configurations were placed on the substrate with periodic boundary conditions and dimension 40a by 40a.

We first consider phases generated starting with rectangular packing. The initial configurations were generated using lattice vectors $\vec{b} = (40a/n)\hat{x}$ and $\vec{c} = (40a/m)\hat{y}$, where $\hat{x}$ and $\hat{y}$ are unit vectors in the x and y directions. Most of the phases generated starting with rectangular packing correspond to

the phases predicted by Frank and van der Merwe (FVM).[6] For n=m<40, a square dislocation array with light-wall dislocations is formed (see figure 2a). For n=m>40, a square dislocation array with heavy-wall dislocations is formed. In agreement with the FVM solution, the lowest energy solutions are square dislocation arrays (n=m). For n=m=40, a pseudomorphic phase with all of the adatoms in fourfold hollow sites can be produced. However the ability to simultaneously relax atomic coordinates in two dimensions allows another strain relief mechanism which is not possible in the FVM theory. This "clock-rotated" phase, shown in figure 2b, has been seen experimentally for various adsorbates on (100) surfaces. For our parameters it was stable for adatom bond lengths in the range between about 1.02a and 1.08a.

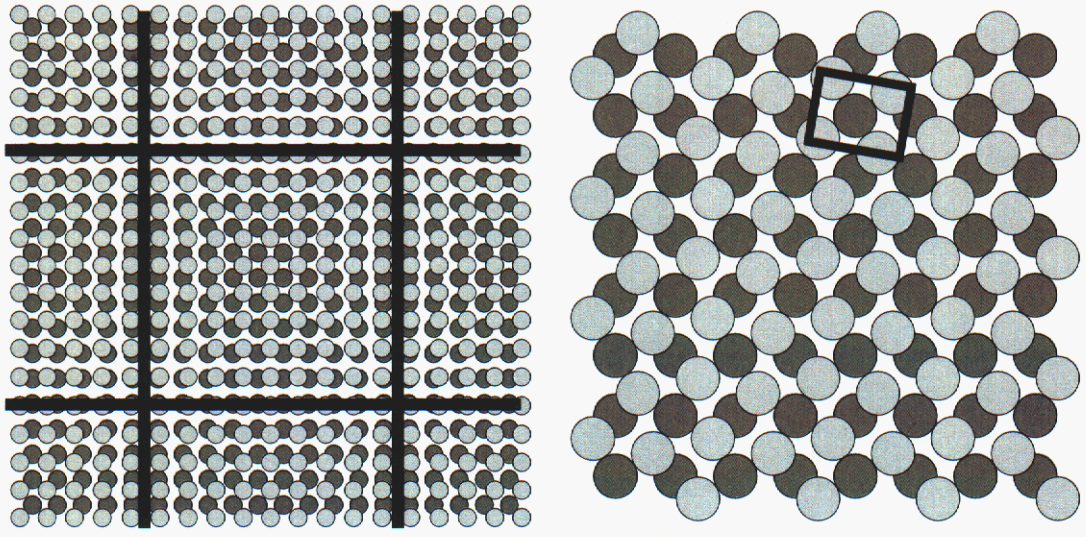

Figure 4-2: Typical structures formed by minimizing the energy of initial structures with rectangular packing. Fig. 4-2a is the square dislocation pattern predicted by Frank and van der Merwe. The dislocations are indicated by the heavy lines. Fig. 4-2b is the clock rotation. Units of four adatoms are rotated clockwise and expanded slightly relative to the pseudomorphic structure. This increases the length of the bonds within the unit of four atoms. It also brings some atoms within a neighboring unit closer.

We next consider phases generated starting with hexagonal packing. The initial configurations were generated using lattice vectors $\vec{\mathbf{b}} = (40a/n)\mathbf{x}$ and $\vec{\mathbf{c}} = (20a/n)\mathbf{x} + (40a/m)\mathbf{y}$, where $\mathbf{x}$ and $\mathbf{y}$ are unit vectors in the x and y directions respectively. This choice of lattice vectors allows the approximately hexagonal array to fit perfectly on the square substrate. The extent to which the arrays are distorted from perfect hexagonal packing is determined by the choice of n and m. (An approximately hexagonal array would have $m \approx 2\sqrt{3}n/3$.) For positive mismatch, phases with m=40 were favored (see figure 3a). I will call these phases registered. For these registered phases all the adatoms lie along parallel lines (horizontal in fig. 3a) containing fourfold hollow and bridge sites. All of the adatoms avoid on-top sites, and are at least a distance of a/2 from the on-top sites. This strong registry to the substrate allows strain relief while avoiding the energetically costly on-top sites. For negative mismatch, phases with m>40 were favored, some adatoms were near on-top sites, and the phase was called unregistered (see figure 3b).

Phases generated with hexagonal packing rotated by small angles relative to the substrate were also considered. The energies of the rotated

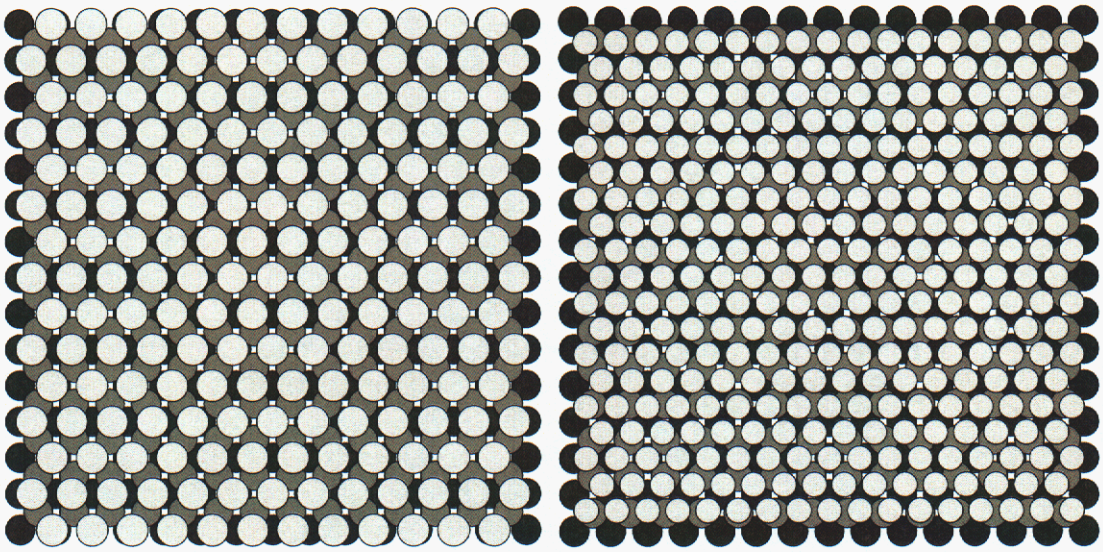

Figure 4-3: Typical structures formed by minimizing the energy of initial structures with hexagonal packing. Fig. 4-3a is a hexagonal structure formed when the overlayer atoms are larger than the substrate atoms (Δ=+0.12). This structure is called registered because the rows of adatoms remain over the fourfold hollow and bridge sites of the substrate. Fig. 4-3b is a hexagonal structure formed when the overlayer atoms are smaller than the substrate atoms (here Δ=-0.16). The structure shown in 4-3b will be called unregistered because some of the adatoms lie near on-top sites.

overlayers were very slightly larger than the energies of unrotated overlayers shown in figure 3. This is in accord with the theoretical predictions from an analytical FK model treating only hexagonal layers.[10] As discussed in reference 10, it appears that rotated overlayers can only be explained in a 2D FK model by allowing higher order terms in the substrate potential.

Once the energy per atom, E, has been calculated as a function of the misfit, Δ, it is straightforward to determine the zero temperature phase diagram by plotting E vs. Δ for the various phases. Because there are so many possible phases, this data is presented in two different plots in figure 4. The upper plot in figure 4 includes only the pseudomorphic and square dislocation phases. Since this plot includes only those phases allowed in the continuum theory of FVM, its predictions agree with that theory. The structure is pseudomorphic for $|\Delta|<0.075$. For larger misfits, square arrays of dislocations form with dislocation spacing decreasing as the misfit increases in agreement with FVM.

In the lower plot of figure 4, E vs. Δ is plotted for the unregistered hexagonal, pseudomorphic, clock-rotated, and registered hexagonal phases. Comparison with the upper plot shows clearly that the clock-rotated and hexagonal phases are lower in energy than square arrays of dislocations over the whole misfit range. The model predicts unregistered hexagonal phases for $-0.2 < \Delta < -0.025$, the pseudomorphic phase for $-0.025 < \Delta < 0.025$, the clock-rotated phase for $0.025 < \Delta < 0.085$, and registered hexagonal phases for $0.085 < \Delta < 0.2$.

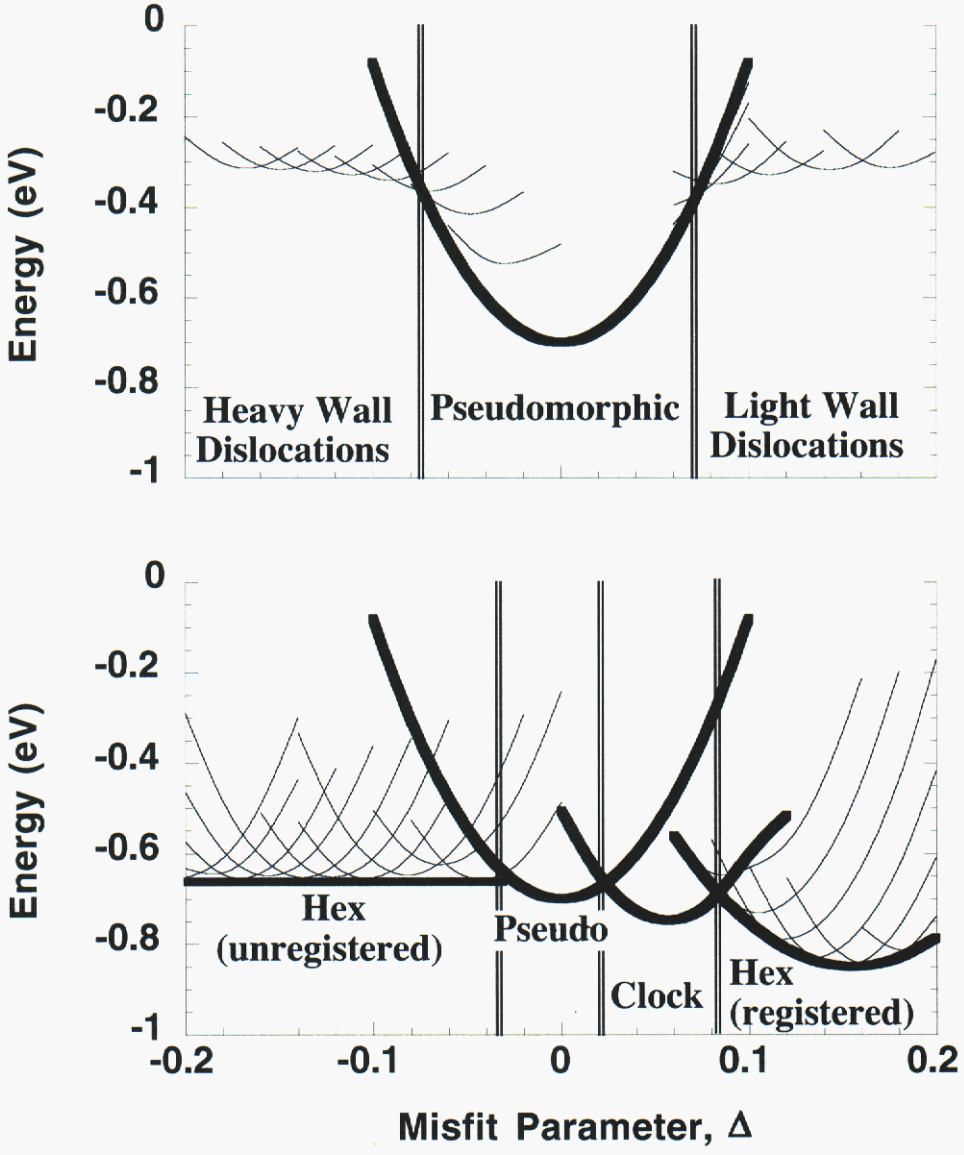

Figure 4: Plot of energy vs. misfit parameter for various possible structures. The upper plot shows only the phases permitted by the FVM model, i.e. pseudomorphic and square dislocation arrays. The lower plot shows the phases which actually have the lowest energy for this model, i.e. unregistered hexagonal, pseudomorphic, clock-rotated, and registered hexagonal. For the registered hexagonal, the phases plotted as light parabolas have n=40, and m=39 (not stable), 38, 37, 36, 35, 34, and 33 respectively. The n=40, m=36 phase is identical to the c(10x2) reconstruction seen for Ag on Cu(100).

The phase diagram will of course depend upon the values chosen for the model parameters. Since the driving force for formation of hexagonal layers is the increase in the adatom-adatom coordination, a fourfold coordinated structure is favored for smaller values of the adatom-adatom binding energy, ε, whereas a sixfold coordinated structure is favored for larger values of ε. The main effect of varying the adatom-adatom potential was found to be shifting the relative energies of the fourfold coordinated and sixfold coordinated structures. Experimentally, metal on metal systems tend to show pseudomorphic, clock and hexagonal structures. I chose the adatom-adatom potential to favor this range of structures.

This model provides a simple and mathematically attractive model of strain relief. There are a number of experimental systems which exhibit phases identical to those predicted by this model. Clean Pt(100), Au(100) and Ir(100) surfaces all exhibit unregistered hexagonal reconstructions.[11] Ni(100 surfaces form a clock-rotated phase upon absorption of one half a monolayer of carbon[2] or nitrogen.[12] Silver atoms absorbed on Ni(100) or Cu(100) exhibit registered hexagonal overlayers with c(2x8) and c(2x10) structures respectively in excellent agreement with this model.[13]

The simple model presented here is intended as a qualitative theory for overlayer strain relief. However it can also be very useful in suggesting structures likely to be found experimentally or in highly-accurate first-principles calculations. For example, one might suspect based on this model that a clock-rotated surface structure should be formed on an fcc (100) metal surface if the bulk sample is subjected to a biaxial compressive strain parallel to the surface. This would be expected because the compressive strain would reduce the bulk lattice constant in the directions parallel to the surface. Thus the effective misfit, Δ, between the surface atoms and the bulk would become positive. I have checked this prediction using the first-principles ultrasoft pseudopotential code, VASP. The initial system was a five-layer Ni slab with two free (100) surfaces. The total number of atoms in the unit cell was 20. Figure 5 shows the total energy of the 20 atom system for the pseudomorphic and the clock-rotated phases plotted as a function of the biaxial compressive strain. This calculation indicates that a nickel (100) surface will reconstruct to the clock-rotated phase for compressive strains exceeding 2.5%. This quantitative LDA calculation is in agreement with the qualitative behavior predicted by the simple 2D FK model. However, the quantitative agreement in the strain at which surface reconstruction occurs is totally fortuitous, depending upon the choice of parameters in the FK model. The success of the model in predicting this previously unexpected reconstruction under biaxial strain suggests that it will be useful in predicting other previously unobserved strain relief phenomena for overlayers on square substrates.

2D Frenkel-Kontorova models have previously been used with great success to model overlayer structures on surfaces with hexagonal symmetry.[14] Strain relief mechanisms for surfaces with square symmetry are quite different from hexagonal surfaces, yet we see here that the 2D Frenkel-Kontorova model provides an suitable model for many of the observed overlayer reconstructions. Parameters for Frenkel-Kontorova models can be derived from first principles calculations providing an important method of simulating overlayer structures in cases where the unit cell is much too large for a complete first principles calculations.

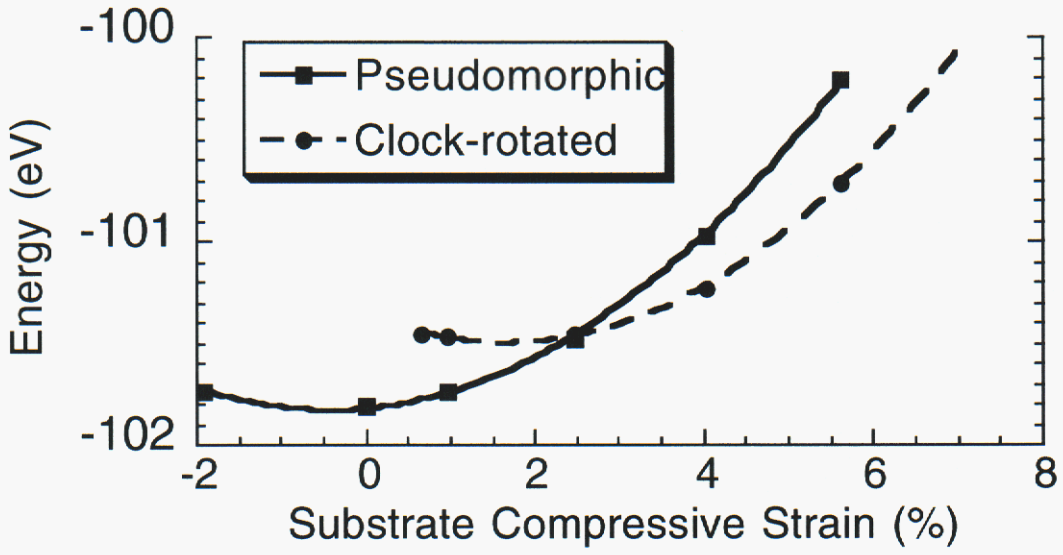

Figure 4-5: First principles LDA calculation for total energy of 5 layer nickel slab subjected to biaxial compressive strain. As the substrate is compressed, the effective misfit between the bulk atoms with their strained lattice constant and the surface layers increases. At about 2.5% strain, the surface layer reconstructs to a clock-rotated structure.

References

1 Y. Fukuda, Y. Kohama, M. Seki, and Y. Ohmachi, Jpn. J. Appl. Phys. 27, 1593 (1988).
2 C. Klink, L. Olesen, F. Besenbacher, I. Stensgaard, E. Laegsgaard and N. D. Lang, Phys. Rev. Lett. 71, 4350 (1993).
3 J. E. Black, D. L. Mills, W. Daum, C. Stuhlmann and H. Ibach, Surf. Sci. 217, 529 (1989)
4 S. G. J. Mochrie, D. M. Zehner, B. M. Ocko and Doon Gibbs, Phys. Rev. Lett. 64, 2925 (1990).
5 B. Müller, B. Fischer, L. Nedelmann, A. Fricke and K. Kern, Phys. Rev. Lett. 76, 2348 (1996).
6 F. C. Frank and J. H. van der Merwe, Phil. Mag. 198A, 216 (1949).
7 B. Dodson, Phys. Rev. Lett. 60, 2288 (1988), N. Takeuchi, C. T. Chan and K. M. Ho, Phys. Rev. Lett. 63, 1273 (1989), X. Wang, Phys. Rev. Lett. 67, 3547 (1991), V. Fiorentini, M. Methfessel, M. Scheffler, Phys. Rev. Lett. 71, 1051 (1993).
8 J. A. Sprague and C. M. Gilmore, Surf. Coatings Technol. 65, 71 (1994).
9 A. Patrykiejew, S. Sokolowski and K. Binder, J. Chem. Phys. 115, 983 (2001).
10 Y. Okwamoto and K. H. Benneman, Surf. Sci. 186, 511 (1987).
11 M. A. VanHove, R. J. Doestner, P. C. Stair, J. P. Biberian, L. L. Kesmodel, and G. A. Somorjai, Surf. Sci. 103, 189, 1981.
12 F. M. Leibsle, Surf. Sci. 297, 98 (1993)
13 A. Brodde, G. Wilhelmi, D. Badt, H. Wengelnik and H Neddermeyer, J. Vac. Sci. Technol. 9, 920 (1991), P. T. Springer, E. Laegsgaard, and F. Besenbacher, Phys. Rev. B. 54, 8163 (1996).
14 S. Narasimhan and D. Vanderbilt, Phys. Rev. Lett. 69, 1564 (1993), J. C. Hamilton and S. M. Foiles , Phys. Rev. Lett. 75, 882 (1995).

This page intentionally left blank

DISTRIBUTION

1	MS 1411	C.C. Battaile, 1834
1	MS 1411	E.A. Holm, 1834
1	MS 1411	S.M. Foiles, 1834
1	MS 1411	H.E. Fang, 1834
1	MS 1415	J.E. Houston, 1114
1	MS 1427	J.M. Phillips, 1100
1	MS 9011	D. Cohen, 8941
1	MS 9161	D.L. Medlin, 8761
1	MS 9161	J.C. Hamilton, 8761
1	MS 9161	N.C. Bartelt, 8761
1	MS 9161	E.-P. Chen, 8763
1	MS 9161	J. Zimmerman, 8763
1	MS 9161	P.A. Klein, 8763
1	MS 9403	K.J. Gross, 8723
1	MS 9404	G. Kubiak, 8750
1	MS 9405	J. Hruby, 8700
1	MS 9405	D.J. Bammann, 8726
1	MS 0323	D. Chavez, LDRD Office, 1011
3	MS 9018	Central Technical Files, 8945-1
1	MS 0899	Technical Library, 9616
1	MS 0612	Classification Office, 8511 for Technical Library MS 0899, 9616 for DOE/OSTI via URL

This page intentionally left blank